Journal of Materials Chemistry A

ROYAL SOCIETY OF CHEMISTRY

PAPER

View Article Online
View Journal | View Issue

Cite this: *J. Mater. Chem. A*, 2021, **9**, 23140

Cotton cloth supported tungsten carbide/carbon nanocomposites as a Janus film for solar driven interfacial water evaporation†

Bojing Sun,[a] Yun Han,[a] Siwei Li, *[a] Ping Xu, [a] Xijiang Han,[a] Ayman Nafady,[c] Shengqian Ma *[b] and Yunchen Du *[a]

Received 7th August 2021
Accepted 24th September 2021

DOI: 10.1039/d1ta06707a

rsc.li/materials-a

Solar-driven interfacial water evaporation, a sustainable approach to overcome the global freshwater shortages, requires both robust solar absorber materials and an effective evaporation structure. Herein, tungsten carbide/carbon nanocomposites from a solvent-free synthesis are chosen as the solar absorber materials and uniformly attached on the surface of cotton cloth to construct a water evaporation film. The ultrafine size and good dispersion of tungsten carbide nanoparticles on carbon nanosheets can realize the utilization of the full solar spectrum (200–2500 nm). More importantly, the resultant film exhibits completely different properties on its two sides, where the side with tungsten carbide/carbon nanocomposites is highly hydrophobic and can dispel water vapor and alleviate condensation, while the other side, without any modification, has superhydrophilicity and low thermal-conductivity helpful to re-dissolve salt crystals and prevent heat loss. Thanks to the compatible advantages of tungsten carbide/carbon nanocomposites and cotton cloth, the evaporation rate of the optimal film is 1.58 kg m^{-2} h^{-1} under one sun illumination, which can be further raised to 2.53 kg m^{-2} h^{-1} if the film is folded into a pyramidal configuration. Significantly, it can retain stable performance through 10 evaporation cycles and is even suitable for considerable evaporation in sewage. We believe this work will provide new insights for the design and fabrication of interfacial water evaporation devices.

1. Introduction

The shortage of water resources has triggered growing enthusiasm to develop economical and sustainable methodologies for the purification of brine or wastewater.[1–3] Solar-driven water evaporation, which is one of the most promising approaches to obtain high-quality freshwater, is receiving extensive attention in both academia and industry.[4–6] Among various solar-driven desalination systems, interfacial water evaporation is drastically attractive because it can achieve high evaporation rates with low photothermal materials *via* localizing the heat to the working area.[7–9] It is worth noting that the efficiency of an interfacial evaporation system is not only determined by the intrinsic physico-chemical properties of solar absorbers, but also depends on the structure of evaporation films.[10]

Carbon materials benefitting from their excellent light harvesting have always been recognized as a kind of powerful candidate for solar absorbers.[11–13] However, their relatively high thermal emittance will cause an unnecessary heat loss, thereby leading to a notable decrease in photothermal conversion efficiency (PCE).[10,14] Nanoscale plasmonic absorbers have demonstrated their good thermal energy conversion capability, and can even exhibit ultrahigh light absorption equivalent to carbon materials.[15,16] Therefore, introducing some secondary components with unique local surface plasmon resonance (LSPR) and

[a]*MIIT Key Laboratory of Critical Materials Technology for New Energy Conversion and Storage, School of Chemistry and Chemical Engineering, Harbin Institute of Technology, Harbin 150001, China. E-mail: yunchendu@hit.edu.cn; swli@hit.edu.cn; Fax: +86-451-86418750; Tel: +86-451-86413702*

[b]*Department of Chemistry, University of North Texas, 1508 W Mulberry St, Denton, TX 76201, USA. E-mail: Shengqian.Ma@unt.edu*

[c]*Department of Chemistry, College of Science, King Saud University, Riyadh 11451, Saudi Arabia*

† Electronic supplementary information (ESI) available: Experimental section; XPS spectra, TG curves, TEM images, and SAED patterns of WC/C-*n*; AFM image and the corresponding height profiles of WC/C-3; optical and SEM images of pristine cotton cloth and JF-3; camera photos of the water droplet impregnation process on the pristine surface, PVDF coating surface and WC/C-3 coating surface of JF-3; crystal structure models; phonon band structure and density of states; models for FDTD simulation with different diameters; solar-to-water conversion efficiencies; water evaporation rates of RGO JF, WC/C-1@RGO JF, WC/C-2@RGO JF and JF-3; electric field distribution of WCNPs with different inner-particle distances; IR images of JF-3; optical and IR images of the single pyramidal evaporator and pyramid-array evaporator; water evaporation flux evolution of the pyramidal evaporator; water evaporation performance of evaporators with different configurations; XRD pattern and TEM images of WC/C-3 after ten hours of illumination; optical image of the liquid water collection device; comparison of photos of the pollutant solution before and after evaporation; XRD patterns, TEM images, surface temperature changes, and water evaporation flux evolution of MoC/C and VC/C. See DOI: 10.1039/d1ta06707a

low thermal emittance into carbon materials is a popular strategy to improve PCE, as these nanoscale plasmonic materials may exhibit strong thermal energy conversion capability and reduce heat loss.[10,17] So far, carbon-based nanocomposites with desired noble metal nanoparticles, such as Au and Ag, have demonstrated very high PCEs in interfacial water evaporation, but the high cost and scarcity of the noble metals have largely limited their widespread utilization.[18,19] Recent progress indicates that it is of great interest to develop non-noble nanocomposites to excite interfacial water evaporation.[20–22] For example, Huang *et al.* enhanced the PCE of N-doped graphene urchins from 66.5 to 81.7% by *in situ* embedding Cu nanodots, which could account for an obvious temperature increase from room temperature to 70 °C in 600 s under a simulated solar light through an intensive LSPR effect.[23] It is unfortunate that such metal nanoparticles easily suffer from fusion together and dissolution/desorption at relatively high temperature, unless a protective shell layer is created on their surface.[1] Compared with these metal-based plasmonic absorbers, transition metal carbides (TMCs) with desirable photothermal conversion capability and remarkable temperature resistance have shown great potential in photothermal catalysis and therapy.[24–26] Sun *et al.* firstly manifested that a tungsten carbide (WC) nanoarray film could indeed produce efficient water evaporation performance through a precise design on discrete hydrophobic and hydrophilic domains.[27] Thus, it could be anticipated that the combination of carbon and TMCs may lead to a significant breakthrough for interfacial water evaporation, while the related studies are still inaccessible.

Apart from solar absorbers, the structure of the evaporation film also plays a key role in interfacial water evaporation.[1] In principle, an ideal evaporation film should have three distinct characteristics on the surface in contact with water, namely thermal insulation, hydrophilicity, and porosity. In this respect, thermal insulation will intensively localize heat at the film/water interface, and hydrophilicity and porosity will facilitate water supply and suppress the precipitation of salt crystals. Hence, great efforts have been devoted by pioneering research groups to fulfill these demands through designing and manipulating the structure of evaporation films.[28,29] For example, Singamaneni *et al.* assembled a bi-layered hybrid biofoam through a long-time (*ca.* 15 d) and a complicated incubation of graphene oxide and nanocellulose in bacterial medium;[30] Chen *et al.* pertinently arranged three functional layers from top to bottom, where a copper sheet coated with cermet (BlueTec eta plus), a polystyrene foam disk, and a sheet of large transparent bubble wrap have been used to reduce convective, conductive, and radiative heat loss.[31] Although these impressive structure designs promise obvious improvements in PCE, the complex preparation processes have hampered their practical application. Thus, it remains challenging yet highly desirable to construct a high-performance solar evaporation film in a simple manner.

Herein, we employ tungsten carbide/carbon (WC/C) nanocomposites, from a solvent-free strategy, as solar absorbers. After loading them on a commercially available cotton cloth, the as-prepared film exhibits quite different properties on its two sides (Scheme 1), where the pristine side of cotton cloth is superhydrophilic and adiabatic, while the other side with WC/C nanocomposites is highly hydrophobic with a full solar spectrum absorption. Evaporation experiments show that this Janus film can achieve an evaporation rate of 1.58 kg m^{-2} h^{-1}, and its performance can be further reinforced through rational configuration design. We believe that the facile approach developed in this study will inspire further synthesis and fabrication of an efficient interfacial water evaporation film.

2. Results and discussion

The typical synthesis process of the WC/C Janus film is schematically illustrated in Fig. 1a. Ammonium metatungstate (AMT) and dicyandiamine (DCA) were ground in an agate mortar thoroughly for 20 min, and then the solid mixture was pyrolyzed at 800 °C under a N_2 atmosphere. The products were denoted as WC/C-*n* where *n* is the weight ratio of DCA to AMT ranging from 0.3 to 5.0. Finally, WC/C-*n* nanocomposites were coated on the surface of cotton cloth with PVDF as the binder to form an interfacial water evaporation film. The resultant Janus film was further denoted as JF-*n*, where *n* refers to the sample of WC/C-*n* in the corresponding film. The specific experimental details are provided in the ESI.†

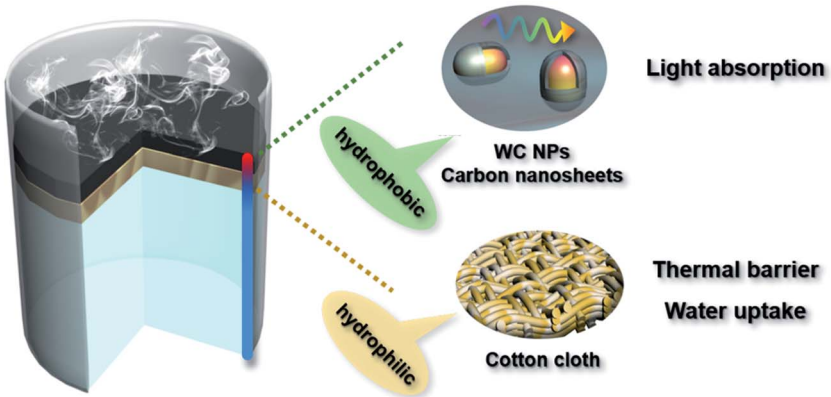

Scheme 1 Schematic illustration of the structure of the solar-driven water evaporation film.

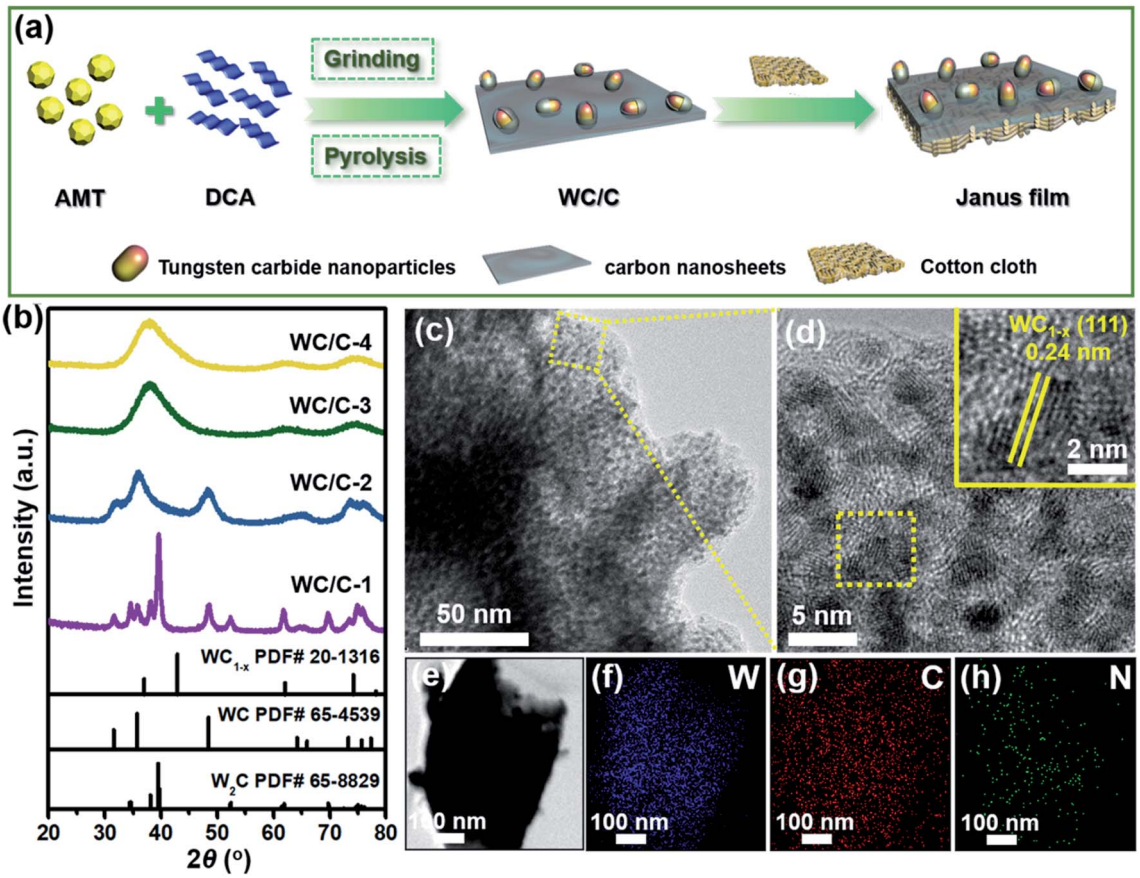

Fig. 1 Schematic illustration of the synthesis process of JF-*n* (a), XRD patterns of WC/C-*n* (b), TEM images of WC/C-3 (c and d), and elemental mapping of W, C and N elements from WC/C-3 (e–h). The inset in (d) is the HR-TEM image of WC/C-3.

Fig. 1b shows the X-ray diffraction (XRD) patterns of the as-synthesized WC/C-*n* nanocomposites. It is interesting to see that the weight ratio of DCA to AMT can greatly affect the crystalline phase of tungsten carbide particles. With the lowest DCA/AMT ratio of 0.3 in the solid mixture, WC/C-1 consists of both close-packed hexagonal W_2C (PDF# 65-8829) and hexagonal WC (PDF# 65-4539) phases.[32] When the DCA/AMT ratio increases to 1.0, all characteristic peaks associated with the W_2C phase have disappeared, and the remaining peaks can be well matched with the WC phase, indicating the formation of single-phase tungsten carbide particles in WC/C-2. WC/C-3 with a DCA/AMT ratio of 3.0 again displays a different XRD pattern, whose characteristic peaks at 37.0°, 62.0° and 74.2° can be precisely matched with the (111), (220) and (311) planes of face-centered cubic WC_{1-x} (PDF# 20-1316), respectively.[33,34] These results are in good agreement with an argument in a previous study that a high carbon environment will be favorable for the generation of WC_{1-x}.[35] X-ray photoelectron spectroscopy (XPS) is further employed to confirm the composition of the as-synthesized samples. As seen in the N 1s spectrum of the samples (Fig. S1†), there is only one peak belonging to the N–C bond at 401.5 eV, while the peak for N-metal at 397.0 eV cannot be detected.[36–38] On the other hand, the binding energy of W $4f_{7/2}$ is gradually increased from about 31.2 to 31.6 eV with the increase of carbon content. These values are consistent with the reported binding energies of W $4f_{7/2}$ of tungsten carbides (31.2 to 31.9 eV).[34,39,40] In contrast, the binding energy of W $4f_{7/2}$ of tungsten nitride is usually reported to be 32.3–32.8 eV, which is significantly larger than that of tungsten carbide due to the higher electronegativity of the N atom than the C atom.[38,41] These results directly exclude the possibility of the existence of WN_x and WC_xN_y in these composites. In addition to different XRD patterns, one can also observe that these characteristic peaks are broadened from WC/C-1 to WC/C-3, suggesting that the average size of tungsten carbide particles decreases gradually.[42] Although further increasing the DCA/AMT ratio will not change the XRD pattern of tungsten carbide particles any more, thermogravimetric (TG) analysis reveals that a high DCA/AMT ratio may result in an increase in the carbon content of these WC/C-*n* nanocomposites (Fig. S2†).

Transmission electron microscopy (TEM) measurement is further carried out to investigate the microstructure of these nanocomposites. It is clear that tungsten carbide particles in WC/C-1 show two distinct features: some ultrafine nanoparticles (~5 nm), which are uniformly deposited on the nanosheets, and the rest of the nanoparticles have random size and agglomerate together without the support of carbon nanosheets (Fig. S3†). This is because the content of carbon nanosheets is relatively low, and thus they cannot accommodate excessive WCNPs. HR-TEM images record two different

lattice fringes in WC/C-1, 0.24 and 0.25 nm, which correspond to the (200) plane of W_2C and (100) plane of WC, respectively.[43] The selected area electron diffraction (SAED) pattern of WC/C-1 also shows diffraction rings that belong to W_2C and WC (Fig. S3f†), respectively. These results again verify that WC/C-1 consists of WCNPs with two different phases, in good agreement with the XRD patterns. It is of note that these disordered nanoparticles disappear in WC/C-2, and all nanoparticles with the average size of 5–6 nm are densely supported by carbon nanosheets (Fig. S4a and b†). The lattice fringe of 0.25 nm can be associated with the (100) plane of WC (Fig. S4c†). With further increasing the DCA/AMT ratio, one can easily notice that the deposition density of WCNPs in WC/C-3 is not as dense as that in WC/C-2, given that their average particle size decreases to 3–4 nm (Fig. 1c and d). The lattice fringe also changes from 0.25 to 0.24 nm (Fig. 1d, inset), suggesting the phase transformation from hexagonal WC to face-centered cubic WC_{1-x}.[44] The distribution of WCNPs gets slightly thinner in WC/C-4, while this change does not affect the particle size and crystalline structure obviously (Fig. S5†). Atomic force microscopy (AFM) is also utilized to characterize the morphology of WC/C-*n* nanocomposites. As shown in Fig. S6,† the thickness of WC/C-3 measured from different regions varies in a very small range of 6.5–8.2 nm, which is slightly larger than the average size (3–4 nm) of WCNPs, confirming that WCNPs are uniformly dispersed on ultrathin carbon nanosheets. The results of elemental mapping (Fig. 1e–h) clearly validate the homogeneous distribution of W atoms, and they can even produce an identical distribution profile to that of C atoms. Moreover, N element is evenly distributed on the carbon nanosheet, which is consistent with the results of XPS. However, the electron beam cannot be focused as small as WCNPs, and thus elemental mapping images cannot distinguish their shapes. For the same reason, the SAED patterns of WC/C-2, WC/C-3, and WC/C-4 fail to provide discernible diffraction rings (Fig. S7†).

The evaporation film is fabricated by coating WC/C-*n* nanocomposites on the upper surface of cotton cloth. The color change, as illustrated by the optical images, suggests the successful coating process (Fig. S8†). Scanning electron microscopy (SEM) images reveal that the pristine cotton cloth is composed of loose and smooth cotton microfibers (Fig. S9†). The coating process not only makes gaps among cotton microfibers full of WC/C-*n* nanocomposites, but also drives the attachment of WC/C-*n* nanocomposites on the surface of cotton microfibers. The SEM image also reveals that WC/C mainly disperses on one side of the cotton cloth, and the other side still retains the original structure (Fig. S10†), implying that there will be different properties on both sides. Taking JF-3 as an example, the surface wetting properties of JF-3 are also measured (Fig. S11†). Under ambient conditions, a water droplet can quickly spread across the surface of cotton cloth within 1 s. This phenomenon indicates that the pristine surface of cotton cloth is super hydrophilic, which is quite beneficial to water supplement during the evaporation process.[45,46] In contrast, the other side with pure PVDF and WC/C-3 shows good hydrophobicity, and the water droplet can maintain large contact angles of 116.0° and 134.0°, respectively, even after 180 s. As a result, this evaporation film can float on the water surface to prevent heat loss, and more importantly, the hydrophobic surface can drive the removal of condensate water droplets spontaneously through a jumping motion,[47,48] which alleviates the negative effect of condensation on water vapor transfer significantly.

The efficiencies of solar absorption and solar-heat conversion are very crucial for interfacial water evaporation. The light properties of WC/C are investigated by UV-vis-NIR diffuse reflectance spectroscopy. As shown in Fig. 2a, all WC/C nanocomposites have ultrahigh light absorption in the wavelength range of 200–2500 nm. The surface temperatures of JF-1, JF-2, JF-3, and JF-4 can reach 38.6, 44.5, 47.9, and 48.8 °C under 1 sun illumination after 1 h, respectively, much higher than that of 3.5 wt% NaCl solution alone (31.7 °C) (Fig. 2b and c). To understand the photothermal conversion mechanism of tungsten carbide, we employed first-principles calculation methods to study the phonon dispersion relations and the corresponding phonon densities of states (DOS) of W_2C, WC and WC_{1-x}. The structural models of W_2C, WC and WC_{1-x} applied for theoretical calculation are shown in Fig. S12.† It can be seen from Fig. 2d and S13† that the optical phonon bands possess a finite linewidth throughout the entire Brillouin zone, which indicates that there is a strong interaction between phonons and electrons. Compared with W_2C and WC, WC_{1-x} displays superior electron–phonon coupling as identified by its high phonon frequency (~105 meV) and large linewidths.[49] In this study, Finite Difference Time Domain simulation (FDTD simulation) is also adopted to analyze the optical absorption characteristics of WCNPs with different sizes, and the model for FDTD simulation is shown in Fig. S14.† The optical characteristics of a single WCNP with a diameter of 50 nm and a group of WCNPs with an average diameter of 5 nm are calculated under incident light irradiation (wavelength: 550 nm) using optical simulation (Fig. 2e and f). The results clearly suggest that the electric field between small WCNPs is drastically intensified as compared with that around a single large WCNP. This phenomenon proves that WCNPs cause the hybridization effect of LSPR, and WCNPs with small size may have better optical absorption and photothermal conversion efficiency. FDTD simulation at various wavelengths (300–800 nm) shows that the LSPR peak of WCNPs with small size centers at about 550 nm (Fig. 2g), and it still has an obvious effect on the near infrared region. All of the above results suggest that WC/C-3 and WC/C-4 have great potential to produce excellent photothermal conversion efficiency. Infrared (IR) images are further employed to study the temperature distribution, which is important for interfacial water evaporation films.[50] The top view indicates a homogeneous distribution of temperature in the *xy* plane, meaning that WC/C-3 is homogeneously coated on cotton cloth (Fig. 2h). Significantly, in the *z* axis, the "hot area" is at the interface between cotton cloth and water owing to the extraction heat-insulating properties of cotton (the thermal conductivity of cotton cloth is only 0.05 W m^{-1} K^{-1}) (Fig. 2i). For comparison, the homogeneous distribution of temperature is observed in the blank control experiment. Based on these results, it can be concluded that the fabricated Janus film can effectively convert

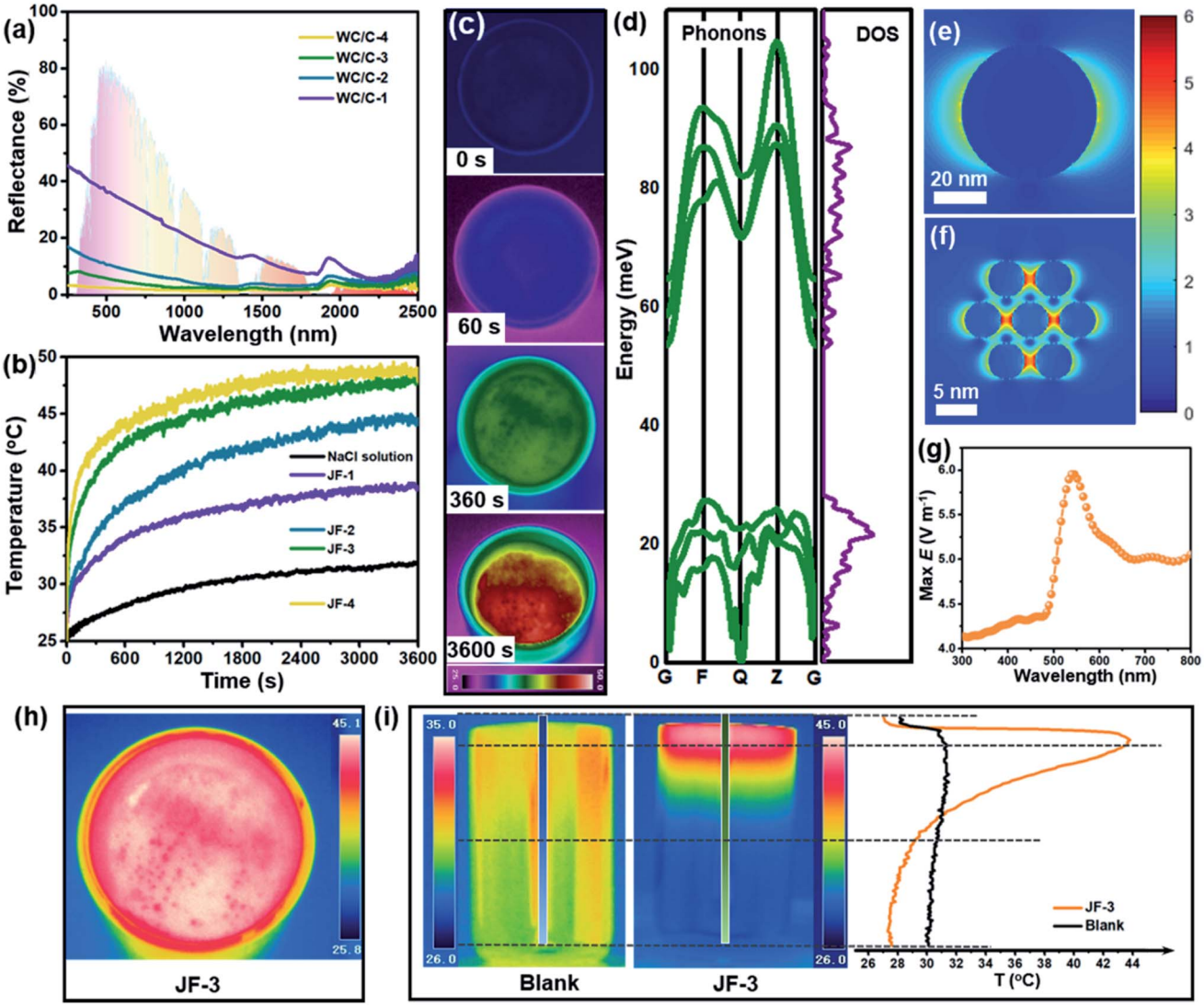

Fig. 2 UV-vis-NIR spectra of WC/C-*n* nanocomposites (a). Time-dependent surface temperature changes of 3.5 wt% NaCl solution without and with the aid of the Janus evaporation film (b). IR images of surface temperature of JF-3 under 1 sun solar illumination at various time points (c). Phonon band structure and density of states of WC_{1-x} (d). FDTD calculated electric field distribution of WC with different sizes under 550 nm light input (e and f), and max electric field intensities of WC/C-3 under different light inputs (g). IR images of the top surface for JF-3 and side face, and temperature profiles of the water–air interface without and with JF-3 under light irradiation for 30 min (h and i).

solar energy to heat and localize the heat at the interface for water evaporation as well.

The outstanding light absorption and thermal management of JF may provide a unique opportunity for highly efficient photothermal evaporation systems. Then, the solar-driven water evaporation performances of JF-*n* are evaluated under 1 sun irradiation. The water evaporation rates were calculated with the data recorded using a precise analytical balance. As seen in Fig. 3a, the evaporation rate of NaCl solution alone is only 0.35 kg m^{-2} h^{-1}. Once the Janus films are introduced, the evaporation rate will be drastically increased by 3–5 fold, and the corresponding solar-to-water conversion efficiency is shown in Fig. S15.† Specifically, from JF-1 to JF-3, the evaporation rate increases gradually and reaches the highest value of 1.58 kg m^{-2} h^{-1}, which is at the top level as compared with those of some excellent evaporation films reported (Fig. S16†). In principle, the improvement in evaporation rate may be attributed to a plethora of parameters such as the carbon content, the crystalline phase of WCNPs, and the microstructure nature of WC/C nanocomposites. Although WCNPs have a good LSPR effect,[27,51] they can only raise the temperature closely around WCNPs and fail to diffuse the heat due to poor thermal conductivity of TMCs.[52,53] The introduction of carbon nanosheets promotes the diffusion of photo-generated heat to a great extent, thus enhancing the evaporation rate. Considering that it is impossible to adjust the crystalline phase of WCNPs without changing the carbon content, we have to artificially introduce RGO to supplement the carbon content of WC/C-1 and WC/C-2 on the basis of TG curves obtained for WC/C-3 to roughly evaluate the influence of the crystalline phase. The results manifest that although the

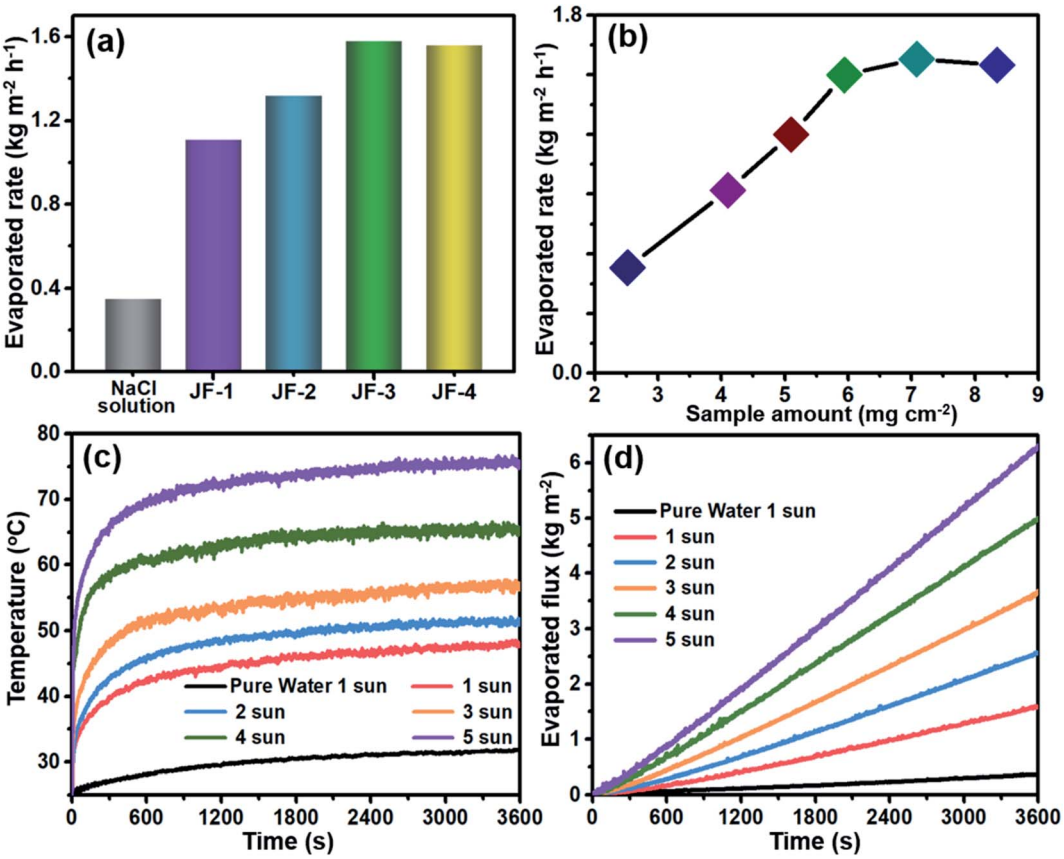

Fig. 3 Water evaporation rates of 3.5 wt% NaCl solution without and with the aid of the Janus evaporation film (a). Influence of the loading amount of WC/C-3 on the water evaporation rate (b). Surface temperature changes (c) and water evaporation flux evolution (d) of 3.5 wt% NaCl saline water without and with the aid of JF-3 under different irradiation powers.

evaporation rate of RGO JF is poor, RGO indeed reinforces the evaporation rates of JF-1 and JF-2; however, they are still lower than that of JF-3 (Fig. S17†). Therefore, it may be concluded that WCNPs play an important role in improving the evaporation rate of JF, and WC_{1-x} is more active than W_2C and WC for interfacial water evaporation, which is also consistent with the calculated results of phonon spectra. Besides, the inter-particle distance is another important factor that affects the LSPR effect of WCNPs.[51] TEM images reveal that the inter-particle distance of WCNPs in these composites gradually becomes large with the increase of carbon content (Fig. 1d, S4 and S5†). Therefore, we further simulate the optical properties of different WC/C-*n* nanocomposites with artificially designated inter-particle distances of 1.0, 1.5, and 2.0 nm (Fig. S18†). The distribution of electric field intensity indicates that the LSPR effect will reach the maximum when the inter-particle distances is at 1.5 nm. That is to say, either overstacking or high dispersion of WCNPs may weaken their LSPR effect to some extent, and thus the excellent evaporation rate of JF-3 not only benefits from the synergistic advantage of active WC_{1-x} nanoparticles and high thermal conductivity of carbon nanosheets, but also from the strong LSPR effect of WCNPs generated by their moderate inter-particle distance.

The effects of related experimental parameters on the evaporation rate of JF-3 are also investigated. As the loading amount of WC/C-3 nanocomposites increases, the evaporation rate and solar energy efficiency also increase gradually and stabilize at 1.50–1.58 kg m^{-2} h^{-1} and 90–93% finally (Fig. 3b and S19†). However, a larger loading amount cannot promise a higher evaporation rate, and instead, it could present a side effect on interfacial water evaporation. This phenomenon is still determined by the balance between photothermal conversion and thermal emittance. A large loading amount means that more WC/C-3 nanocomposites are accumulated on the surface of cotton cloth, resulting in excessive thickness of the light absorber (Fig. S10†), which will lead to rapid thermal emittance caused by the fact that the photo-generated heat cannot be transferred to interfacial water in time, affecting the upward diffusion of water vapor. Therefore, an excessive loading amount and thickness of WC/C-3 will not be conducive to the evaporation rate of JF-3. Light intensity is another critical factor that can affect the evaporation rate.[11] As shown in Fig. 3c and S20,† when the irradiation power is manipulated from 1 to 5 suns, the surface temperature of JF-3 increases from 47.9 to 75.8 °C. More importantly, the total mass of evaporated water not only shows a linear dependence on the irradiation time, but also proportionally increases with the irradiation intensity (Fig. 3d). These results again verify that JF-3 has excellent photothermal conversion capability and allows highly efficient solar-steam conversion. Recent progress shows that there is great interest in further improving the evaporation rate of

various photothermal films through rational configuration design.[8–10,31] Prompted by this trend, we further fold JF-3 into a pyramidal configuration (Fig. S21†). A pyramidal configuration evaporator can effectively enlarge the area of water evaporation and light absorption, and thus enhance the light-harvesting capacity compared with a 2D flat film. In addition, common conical evaporators usually fail to allow full utilization of the water evaporation area due to the gap among cones. Therefore, a pyramidal configuration evaporator can evidently improve the evaporation rate. Thermal imaging maps disclose that the temperature difference between the top and bottom of each pyramid is small (less than 7 °C), and the thermal insulation effect at the interface between the pyramid and water remains good (Fig. S22†). With this configuration design, the evaporation rate of the pyramidal device can reach up to 2.53 kg m^{-2} h^{-1} under one sun illumination thus establishing its superiority to some high-performance evaporators with different configurations (Fig. S23 and S24†).

Long-term durability usually determines the practical application prospects of the water evaporation film. JF-3 gives

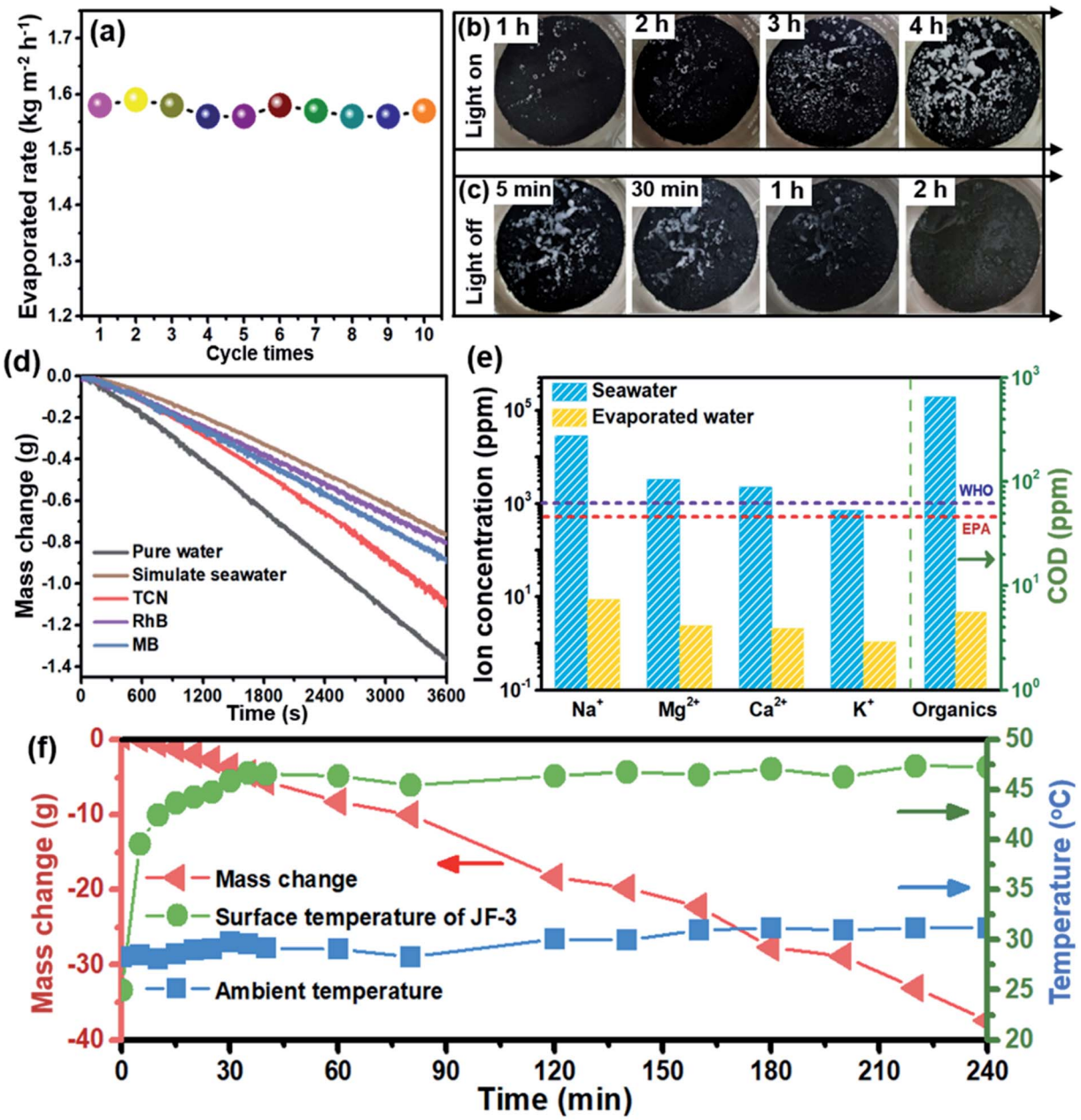

Fig. 4 The stability test (a), and optical images of the salt deposition process (b) and salt dissolution process (c) of JF-3. Time-dependent mass change of water using JF-3 in pure water, simulated seawater, and aqueous solution containing organic pollutants (d). Comparison of the concentrations of ions and organic components in simulated seawater and evaporated water (e). Evaporation mass loss and synchronous changes of the JF-3 surface temperature and ambient temperature under solar irradiation from 11:00 to 14:00 on 13 July 2020 at Harbin Institute of Technology (f).

almost constant water evaporation performance after 10 cycles (Fig. 4a). There are two factors responsible for the outstanding durability, namely the structural stability and the resistance to salt crystallization.[54] No tungsten-related species can be detected in the solution by inductively coupled plasma (ICP) after illumination, proving that tungsten leaching is negligible. Moreover, as seen in Fig. S25 and S26,† both XRD and TEM results indicate that WC/C-3 retains the original chemical composition and microstructure after 10 h of illumination in water, demonstrating its good structural stability. Although the salt residues on the top surface of JF-3 can be seen at the first hour and then continuously grow as time evolves (Fig. 4b), these salt residues gradually disappear once the light is turned off (Fig. 4c). This phenomenon can be further supported by close observation with SEM (Fig. S27†). The self-cleaning characteristic of this Janus film arises from the super hydrophilicity of cotton cloth, which continuously supplies water to the surface of JF-3 and thus re-dissolves the salt crystals into bulk fluid. Considering the structural stability and self-cleaning characteristic, the Janus film can evaporate water by day and dissolve salt by night for practical application.

Practically, it is very important for an interfacial water evaporation film to work in low-quality water systems, such as brine and organic wastewater. Therefore, NaCl solution was replaced by a simulated seawater and organic wastewater containing tetracycline (TCN), Rhodamine B (RhB) or Methylene Blue (MB) (Fig. 4d). The device in Fig. S28† is used to recover the distilled water. Fig. 4e shows that the ion concentrations of Na^+, Mg^{2+}, Ca^{2+}, and K^+ as well as the organic content of simulated seawater are decreased from 6331, 1177, 413, 311, and 9.6 ppm to 8.18, 1.22, 1.25, 1.11, and 0.29 ppm, respectively, which are significantly lower than the drinking water standards defined by the Word Health Organization (WHO) and US Environmental Protection Agency (EPA).[22,55] For the simulated organic wastewater, JF-3 still exhibits satisfactory photothermal water evaporation performance, and the optical photos of TCN, RhB and MB before and after distillation showed that the organic pollutants have been completely decolorized (Fig. S29†).

To further explore the practical application of JF-3, water evaporation experiments are carried out under natural sunlight (from 11:00 to 14:00, 13th of July, 2020, Harbin, China) at ambient temperature and humidity. As shown in Fig. 4f, we record the outdoor ambient temperature and the corresponding surface temperature of JF-3, as well as the evaporation mass simultaneously. After about 30 minutes of sunlight irradiation, the surface temperature of JF-3 reaches 45–50 °C, which is obviously higher than the ambient temperature (~30 °C). Then the surface temperature generally remains unchanged, while the water mass decreases linearly, suggesting that the interfacial evaporation film runs smoothly in a realistic environment. The results also confirmed that the occasional clouds in fair weather will not affect the water evaporation performance. The average water evaporation rate of 1.45 kg m^{-2} h^{-1} is achieved for the outdoor experiment, reaching over 90% of the value obtained in the laboratory (1.58 kg m^{-2} h^{-1}). This finding clearly demonstrates that this easily folded and portable Janus film has considerable potential for practical interfacial water evaporation. Importantly, this simple strategy for Janus film is not limited to WC/C nanocomposites. Thus, if AMT is replaced by ammonium molybdate tetrahydrate or ammonium metavanadate, both MoC/C and VC/C nanocomposites will be harvested as illustrated in Fig. S30.† As can be seen in Fig. S31 and S32† both MoC and VC have good dispersion and very small particle size. After being attached on the surface of cotton cloth, both of them exhibited excellent photothermal conversion efficiency and water evaporation performance, suggesting the generality of this strategy for interfacial water evaporation films (Fig. S33 and S34†).

3. Conclusion

In summary, a series of WC/C nanocomposites with adjustable chemical composition and crystalline phases have been successfully prepared by a facile solvent-free method. By loading WC/C nanocomposites on commercial cotton cloth, an excellent evaporation rate and remarkable stability are achieved under one sun illumination. The low-cost film has a desirable self-cleaning characteristic and retains its performance in practical water systems like brine and organic wastewater. This work will pave a new avenue for the design of efficient interfacial water evaporation films, and the simple synthesis method can also be used in the fields of catalysis and energy storage.

Conflicts of interest

The authors declare that they have no conflicts of interest.

Acknowledgements

This work was supported by financial support from the National Natural Science Foundation of China (21676065). The authors also extend their sincere appreciation for the Researchers Supporting Project (no. RSP-2021/79) at King Saud University, Riyadh, Saudi Arabia for partially funding this work.

References

1 P. Tao, G. Ni, C. Song, W. Shang, J. Wu, J. Zhu, G. Chen and T. Deng, *Nat. Energy*, 2018, **3**, 1031–1041.
2 Y. Yang, X. Yang, L. Fu, M. Zou, A. Cao, Y. Du, Q. Yuan and C. Yan, *ACS Energy Lett.*, 2018, **3**, 1165–1171.
3 A. H. Cavusoglu, X. Chen, P. Gentine and O. Sahin, *Nat. Commun.*, 2017, **8**, 311–323.
4 G. Liu, J. Xu and K. Wang, *Nano Energy*, 2017, **41**, 269–284.
5 L. Li, T. Hu, A. Li and J. Zhang, *ACS Appl. Mater. Interfaces*, 2020, **12**, 32143–32153.
6 Y. Pang, J. Zhang, R. Ma, Z. Qu, E. Lee and T. Luo, *ACS Energy Lett.*, 2020, **5**, 437–456.
7 X. Hu and J. Zhu, *Adv. Funct. Mater.*, 2019, **30**, 1907234.
8 Y. Shi, R. Li, Y. Jin, S. Zhou, L. Shi, J. Chang, S. Hong, K. C. Ng and P. Wang, *Joule*, 2018, **2**, 1171–1186.
9 N. Xu, X. Hu, W. Xu, X. Li, L. Zhou, S. Zhu and J. Zhu, *Adv. Mater.*, 2017, **29**, 1606762.

10 H. Liu, Z. Huang, K. Liu, X. Hu and J. Zhu, *Adv. Energy Mater.*, 2019, **9**, 1900310.
11 T. Hu, L. Li, Y. Yang and J. Zhang, *J. Mater. Chem. A*, 2020, **8**, 14736–14745.
12 L. Li and J. Zhang, *Nano Energy*, 2021, **81**, 105682.
13 Y. Yang, R. Zhao, T. Zhang, K. Zhao, P. Xiao, Y. Ma, P. M. Ajayan, G. Shi and Y. Chen, *ACS Nano*, 2018, **12**, 829–835.
14 K. Mizuno, J. Ishii, H. Kishida, Y. Hayamizu, S. Yasuda, D. N. Futaba, M. Yumura and K. Hata, *Proc. Natl. Acad. Sci. U. S. A.*, 2009, **106**, 6044–6047.
15 L. Zhou, Y. Tan, J. Wang, W. Xu, Y. Yuan, W. Cai, S. Zhu and J. Zhu, *Nat. Photonics*, 2016, **10**, 393–398.
16 L. Zhou, Y. Tan, D. Ji, B. Zhu, P. Zhang, J. Xu, Q. Gan, Z. Yu and J. Zhu, *Sci. Adv.*, 2016, **4**, e1501227.
17 X. Zhang, X. Wang, W. D. Wu, X. D. Chen and Z. Wu, *J. Mater. Chem. A*, 2019, **7**, 6963–6971.
18 Z. Sun, J. Wang, Q. Wu, Z. Wang, Z. Wang, J. Sun and C. Liu, *Adv. Funct. Mater.*, 2019, **29**, 1901312.
19 M. Zhu, Y. Li, F. Chen, X. Zhu, J. Dai, Y. Li, Y. Zhi, X. Yan, J. Song, Y. Wang, E. Hitz, W. Luo, M. Lu, B. Yang and L. Hu, *Adv. Energy Mater.*, 2018, **8**, 1701028.
20 S. Ishii, R. P. Sugavaneshwar and T. Nagao, *J. Phys. Chem. C*, 2016, **120**, 2343–2348.
21 F. Yu, X. Min, Y. Xu, Z. Chen, D. Meng, H. Cheng, Z. Shi, P. Shen and X. Wang, *Adv. Mater. Interfaces*, 2019, **6**, 1901168.
22 L. Zhou, Y. Tan, J. Wang, W. Xu, Y. Yuan, W. Cai, S. Zhu and J. Zhu, *Nat. Photonics*, 2016, **10**, 393–398.
23 J. Xu, F. Xu, M. Qian, Z. Li, P. Sun, Z. Hong and F. Huang, *Nano Energy*, 2018, **53**, 425–431.
24 W. Feng, R. Wang, Y. Zhou, L. Ding, X. Gao, B. Zhou, P. Hu and Y. Chen, *Adv. Funct. Mater.*, 2019, **29**, 1901942.
25 C. Song, X. Liu, M. Xu, D. Masi, Y. Wang, Y. Deng, M. Zhang, X. Qin, K. Feng, J. Yan, J. Leng, Z. Wang, Y. Xu, B. Yan, S. Jin, S. Jin, D. Xu, Z. Yin, D. Xiao and D. Ma, *ACS Catal.*, 2020, **10**, 10364–10374.
26 W. Gao, R. Gao, Y. Zhao, M. Peng, C. Song, M. Li, S. Li, J. Liu, W. Li, Y. Deng, M. Zhang, J. Xie, G. Hu, Z. Zhang, R. Long, X. D. Wen and D. Ma, *Chem*, 2018, **4**, 2917–2928.
27 N. Han, K. Liu, X. Zhang, M. Wang, P. Du, Z. Huang, D. Zhou, Q. Zhang, T. Gao, Y. Jia, L. Luo, J. Wang and X. Sun, *Sci. Bull.*, 2019, **64**, 391–399.
28 X. Li, W. Xu, M. Teng, L. Zhou, B. Zhu, S. Zhu and J. Zhu, *Proc. Natl. Acad. Sci. U. S. A.*, 2016, **113**, 13953–13958.
29 S. Yu, Y. Zhang, H. Duan, Y. Lin, X. Quan, P. Tao, W. Shang, J. Wu, C. Song and T. Deng, *Sci. Rep.*, 2015, **5**, 13600.
30 Q. Jiang, L. Tian, K. K. Liu, S. Tadepalli, R. Radiya, P. Biswas, R. R. Naik and S. Singamaneni, *Adv. Mater.*, 2016, **28**, 9400–9407.
31 G. Ni, G. Li, S. V. Boriskina, H. Li, W. Yang, T. Zhang and G. Chen, *Nat. Energy*, 2016, **1**, 1007–1013.
32 A. S. Kurlov and A. I. Gusev, *Inorg. Mater.*, 2006, **42**, 121–127.
33 J. P. Palmquist, Z. Czigany, M. Odén, J. Neidhart, L. Hultman and U. Jansson, *Thin Solid Films*, 2003, **444**, 29–37.
34 A. A. Voevodin, J. P. O'Neill, S. V. Prasad and J. S. Zabinski, *J. Vac. Sci. Technol., A*, 1999, **17**, 986–992.
35 S. E. Mrabet, M. D. Abad, C. López-Cartes, D. Martínez-Martínez and J. C. Sánchez-López, *Plasma Processes Polym.*, 2009, **6**, S444–S449.
36 S. Li, Q. Gu, N. Cao, Q. Jiang, C. Xu, C. Jiang, C. Chen, C. Pham-Huu and Y. Liu, *J. Mater. Chem. A*, 2020, **8**, 8892–8902.
37 S. Li, J. Liu, Z. Yin, P. Ren, L. Lin, Y. Gong, C. Yang, X. Zheng, R. Cao, S. Yao, Y. Deng, X. Liu, L. Gu, W. Zhou, J. Zhu, X. Wen, B. Xu and D. Ma, *ACS Catal.*, 2020, **10**, 907–913.
38 Y. L. Wang, T. Nie, Y. H. Li, X. L. Wang, L. R. Zheng, A. P. Chen, X. Q. Gong and H. G. Yang, *Angew. Chem., Int. Ed.*, 2017, **56**, 7430–7434.
39 S. P. Berglund, H. He, W. D. Chemelewski, H. Celio, A. Dolocan and B. Mullins, *J. Am. Chem. Soc.*, 2014, **136**, 1535–1544.
40 Q. Gong, Y. Wang, Q. Hu, J. Zhou, R. Feng, P. N. Duchesne, P. Zhang, F. Chen, N. Han, Y. Li, C. Jin, Y. Li and S. T. Lee, *Nat. Commun.*, 2016, **7**, 13216.
41 S. Gong, J. Fan, V. Cecen, C. Huang, Y. Min, Q. Xu and H. Li, *Chem. Eng. J.*, 2021, **405**, 126913.
42 B. D. Hall, D. Ugarte, D. Reinhard and R. Monot, *J. Chem. Phys.*, 1995, **103**, 2384–2394.
43 Z. Chen, W. Gong, S. Cong, Z. Wang, G. Song, T. Pan, X. Tang, J. Chen, W. Lu and Z. Zhao, *Nano Energy*, 2020, **68**, 104335.
44 Y. Paulwau and P. Gouy-Pailler, *J. Mater. Res.*, 1992, **7**, 2070–2079.
45 S. Wu, G. Xiong, H. Yang, B. Gong, Y. Tian, C. Xu, Y. Wang, T. Fisher, J. Yan, K. Cen, T. Luo, X. Tu, Z. Bo and K. Ostrikov, *Adv. Energy Mater.*, 2019, **9**, 201901286.
46 Y. Lin, J. Chen, D. Guo, M. Cao and L. Jiang, *ACS Appl. Mater. Interfaces*, 2015, **7**, 13645–13652.
47 N. Miljkovic, R. Enright, Y. Nam, K. Lopez, N. Dou, J. Sack and E. N. Wang, *Nano Lett.*, 2013, **13**, 179–187.
48 J. B. Boreyko and C. H. Chen, *Phys. Rev. Lett.*, 2009, **103**, 184501.
49 D. F. Stefano and L. Johannes, *Phys. Rev. Mater.*, 2019, **3**, 115203.
50 L. Zhu, T. Ding, M. Gao, C. K. N. Peh and G. W. Ho, *Adv. Energy Mater.*, 2019, **9**, 1900250.
51 X. Zhang, H. Wang, M. Wang, Y. Lin and X. Song, *Opt. Express*, 2016, **24**, 22730–22740.
52 M. Xu, *Heat Mass Transfer*, 2021, **57**, 843–852.
53 K. Mensink, E. H. Penilla, P. Martínez-Torres, N. Cuando-Espitia, S. Mathaudhu and G. Aguilar, *J. Mater. Process. Technol.*, 2019, **266**, 388–396.
54 Y. Xia, Q. Hou, H. Jubaer, Y. Li, Y. Kang, S. Yuan, H. Liu, M. W. Woo, L. Zhang, L. Gao, H. Wang and X. Zhang, *Energy Environ. Sci.*, 2019, **12**, 1840–1847.
55 *Safe Drinking-Water from Desalination*. https://www.who.int/water_sanitation_health/publications/desalination_guidance/en/.

